Article

Not peer-reviewed version

Constitutive Modeling of Annealed OFHC with Wide Strain-Rate and Temperature Effects: Incorporating Dislocation Dynamics and Normalized Microstructural Size Evolution

Mengwen Xu , Qianggiang Xiao , Xudong Zu , Yaping Tan , Zhengxiang Huang *

Posted Date: 13 September 2023

doi: 10.20944/preprints202309.0828.v1

Keywords: Constitutive modelling; Microstructural sensitive; OFHC copper; high strain rate

Article

Constitutive Modeling of Annealed OFHC with Wide Strain-Rate and Temperature Effects: Incorporating Dislocation Dynamics and Normalized Microstructural Size Evolution

Mengwen Xu, Qiangqiang Xiao, Xudong Zu, Yaping Tan and Zhengxiang Huang *

School of Mechanical Engineering, Nanjing University of Science and Technology, 200 XiaoLingWei, Nanjing 210094, China

* Correspondence: huangyu@njust.edu.cn (Z. Huang).

Abstract: The flow stress of face-centered cubic (FCC) metals exhibits a rapid increase near a strain rate of 10^4 s^{-1} under fixed strain conditions. However, many existing constitutive models either fail to capture the mechanical characteristics of this plastic deformation or use piecewise strain rate hardening models to describe this phenomenon. Unfortunately, the piecewise models may suffer from issues such as discontinuity of physical quantities and difficulties in determining segment markers, and struggling to reflect the underlying physical mechanisms that give rise to this mutation phenomenon. In light of this, this paper proposes that the abrupt change in flow stress sensitivity to strain rate in FCC metals can be attributed to microstructural evolution characteristics. To address this, a continuous semi-empirical physical constitutive model for FCC metals is established based on the microstructural size evolution proposed by Molinari-Ravichandran and the dislocation motion slip mechanism. This model effectively describes the mutation behavior of strain rate sensitivity under fixed strain, particularly evident in the annealed OFHC. The predicted results of the model across a wide range of strain rates (10^{-4} − 10^6 s^{-1}) and temperatures (77 − 1096 K) demonstrate relative errors generally within ±10% of the experimental values. Furthermore, the model is compared to five other models, including Mechanical Threshold Stress (MTS), Nemat-Nasser-Li (NNL), Preston-Tonks-Wallace (PTW), Johnson-Cook (JC), and Molinari-Ravichandran (MR) models. A comprehensive illustration of errors reveals that the proposed model outperforms the other five models in describing the plastic deformation behavior of OFHC. The error results offer valuable insights for selecting appropriate models for engineering applications and provide significant contributions to the field.

Keywords: constitutive modelling; microstructural sensitive; OFHC copper; high strain rate

1. Introduction

Face-centered cubic (FCC) metals, such as aluminum and copper, are widely utilized in a variety of civil and military applications. However, during processes involving high strain rates and large strains, such as impact, penetration, and deformation processing, these materials exhibit complex nonlinear dynamic mechanical behavior. This behavior encompasses a broad range of strain rates and temperatures, resulting in significant coupling between strain rate, temperature, and strain hardening. Moreover, it is influenced by the historical effects of strain rate and temperature, presenting a formidable challenge in accurately constructing plastic constitutive models. [1–4]

To address these challenges, various dynamic plastic constitutive models have been proposed in recent decades. These models can be classified into two main categories: phenomenological models and models incorporating microstructural evolution. Phenomenological models are purely mathematical and conform to physical laws while possessing simple forms. They require fewer parameters to be calibrated and can produce accurate results within the calibrated range of plastic deformation. The Johnson-Cook (JC) model is one of the most widely used phenomenological constitutive model that consider strain hardening and rate-temperature effects. Modified versions of

 doi:10.20944/preprints202309.0828.v1

the JC model [6–9] have also been proposed using experimental data. However, these models may deviate significantly from reality for plastic deformation beyond the calibrated range of materials.

Experimental studies by Follansbee and Kocks have shown that certain FCC metals, such as annealed oxygen-free high conductivity copper (OFHC), exhibit a sharp increase in flow stress when the strain rate exceeds a critical value (~ 10^4 s^{-1}). Despite the high strain rate, plastic deformation remains dominated by the thermal activation of dislocation motion. This remarkable rate sensitivity is primarily attributed to the microstructural evolution during deformation, which is not accounted for in phenomenological models. Microstructural evolution refers to the changes in the arrangement and characteristics of dislocations at the microscale [11]. These changes can include a rapid increase in dislocation density and a significant decrease in characteristic lengths of dislocations (e.g., dislocation spacing, thermally activated area, cell size), leading to a rapid rise in flow stress [12,13].

In response to the influence of microstructural evolution on material dynamics, several constitutive models have been proposed [12]. These models postulate that the storage distance of dislocations restricts their range of motion, resulting in a limited displacement that dislocations can undergo in unit time. This limitation increases the possibility of interactions between dislocations and defects such as solutes and vacancies, leading to the accumulation and pile-up of more dislocations and enhancing the strain-hardening effect of the material. Examples of such models include the Mecking-Kocks (MK) model [11], Zerilli-Armstrong (ZA) model [14], Mechanical Threshold Stress (MTS) model [10], Nemat-Nasser-Li (NNL) model [15], Gao-Zhang (GZ-1, GZ-2) models [16,2], and Austin-McDowell models [17,18], et al. Among these models, the MTS model captures the mutation phenomenon of strain hardening sensitivity through a single "continuity" equation with Voce law. Similarly, the Preston-Tongs-Wallace (PTW) model adopts an improved Voce strain hardening criterion to characterize the rate-sensitive mutation phenomenon of materials, which is also a single "continuity" equation during the thermal activation stage. On the other hand, the GZ-2 model employs piecewise functions to characterize the sensitivity to strain rate mutations. The abovementioned constitutive models provide valuable insights into the effects of microstructural evolution on the strain hardening behavior of FCC metals, contributing to the development of accurate predictive models.

In addition to phenomenological and microstructure-based models, semi-empirical physical models have also been developed. These models combine experimental data with physical principles and employ empirical parameters or fitting coefficients to simulate the evolution of microstructure-related internal variables. One notable model in this regard is the Molinari-Ravichandran (MR) model [20], which successfully predicts the plastic flow behavior of annealed copper across a wide range of strain rates spanning seven orders of magnitude. The MR model introduces a single internal variable representing the effective microstructural length related to temperature and strain rate, offering valuable insights for metal microstructure design. Other extensions of the MR model are proposed by Durrenberger et al. [21,22], considering the flow stress as the sum of internal stress (long-range interaction) and thermally activated effective stress, providing simplicity and flexibility in describing thermo-viscoplastic behavior under extreme loading conditions.

Motivated by the cell characteristic size evolution mechanism in the MR model, this study develops a simplified semi-empirical physical constitutive model. It utilizes a normalized cell size evolution equation and incorporates the thermal activation of dislocation motion to capture the plastic dynamic mechanical behavior of FCC metals across a wide range of strain rates and temperatures. In this paper, a comprehensive explanation of the theoretical modeling methods for the components of thermal and athermal stresses in the flow stress is presented in Section 2. Section 3 provides the constitutive parameters for annealed OFHC and the sources of experimental values used to validate the predictive capability of the models. Additionally, a comparative analysis is conducted between the proposed model and other mature models, including MTS, NNL, PTW, JC, and MR models, to evaluate their performance in predicting experimental results (Section 4). Finally, the main conclusions are summarized in Section 5.

This study aims to contribute to the advancement of constitutive modeling by capturing the complex behavior of materials during plastic deformation. By incorporating the microstructural

Preprints (www.preprints.org) | NOT PEER-REVIEWED | Posted: 13 September 2023 doi:10.20944/preprints202309.0828.v1

evolution and the thermal activation of dislocation motion, the proposed model provides valuable insights into the dynamic mechanical behavior of FCC metals under various strain rates and temperatures.

2. Constitutive modelling

Plastic flow during the thermally activated motion of dislocations is primarily governed by the movement of dislocations, which will encounter obstacles in the form of short-range and long-range barriers during their motion. Long-range barriers are non-temperature-dependent and are influenced by factors such as grain boundaries, far-field forest dislocations, and other microstructural elements [3,15]. These barriers can impact dislocation motion through mechanisms such as externally applied stress or chemical potential differences. Conversely, the height of short-range barriers is closely related to temperature. At absolute zero temperature (0 K), the height of short-range barriers reaches its maximum value because there is no thermal energy available for dislocations to overcome them. However, the atomic vibration amplitude in the material increases with temperature rising, thereby reducing the height of the short-range barriers. This increase in thermal energy assists dislocations in overcoming the short-range barriers [3]. Therefore, short-range barriers can be overcome through a thermal activation mechanism. In FCC metals, short-range barriers may include forest dislocations, point defects (such as vacancies and self-interstitials), solute atoms, impurities, and precipitates. The presence of these short-range barriers plays a significant role in plastic deformation and the mechanical properties of materials. Thus, based on the nature of barriers and the theory of MTS, the flow stress of a material can be expressed as [10]:

$$\sigma = \sigma_{\text{ath}} + \sigma_{\text{th}} = \sigma_{\text{ath}} + \Phi\left(\dot{\varepsilon}, T\right) \cdot \hat{\sigma}_{\text{th}} \tag{1}$$

where, σ_{ath} represents athermal component of flow stress (rate-independent), which is influenced by material structure properties. σ_{th} represents thermal component of flow stress (rate-dependent), which characterizes the resistance overcome by mobile dislocations through diffusion or slip, driven by thermal activation effects, leading to material plastic deformation. $\hat{\sigma}_{\text{th}}$ is the thermal activation-related mechanical threshold stress at 0 K, and $\Phi\left(\dot{\varepsilon}, T\right)$ is the coefficient of influence related to strain rate and temperature (< 1), indicating the role of thermal activation effects.

2.1. Thermal stress

The thermal stress is closely related to the microstructural features of the material, as it utilizes the thermal vibrations of the crystal lattice to assist dislocations in overcoming weak barriers (such as forest dislocations and Peierls barriers). This facilitates the diffusion or glide of dislocations, resulting in material deformation.

2.1.1. Thermal activation effect in fixed structures

In the mechanism of thermally activated dislocation motion, the average waiting time of dislocations before encountering short-range barriers can be expressed in a modified form of Arrhenius equation [17]:

$$t_{\text{w}} = \frac{1}{\nu_0}\left[\exp\left(\frac{\Delta G}{k_B T}\right) - 1\right] \tag{2}$$

where, ν_0 represents the vibration frequency (~ 10^{11} s^{-1}) of the dislocation before encountering barriers [23], k_B is the Boltzmann constant, T is the temperature, and ΔG is the thermal activation free energy (Gibbs free energy) required for dislocations to overcome the barriers, which is a function associated with the shape of the barrier (e.g., rectangular, square, triangular, parabolic, exponential) as well as stress. The modified form indicates that the waiting time for dislocations in a continuous slip system ($\Delta G = 0$) is zero.

Preprints (www.preprints.org) | NOT PEER-REVIEWED | Posted: 13 September 2023 doi:10.20944/preprints202309.0828.v1

Kocks and Ashby proposed a general expression for activation energy:

$$\Delta G = G_0 \left[1 - \left(\frac{\sigma_{\text{th}}}{\hat{\sigma}_{\text{th}}} \right)^p \right]^q \tag{3}$$

where, G_0 is the reference free energy at 0 K ($= g_0 \mu_0 b^3$, g_0 is the normalized free energy, μ_0 is the shear modulus ($= \mu(0\text{K})$), b is the magnitude of Burgers vector). p and q are a pair of parameters that characterize the shape of the barrier. q corresponds to the shape of the short-range barrier, where for a quasi-parabolic barrier, the range is $1 \le q \le 2$. p describes the rate of decay of the field at longer distances, with a value of $0 < p \le 1$. A value of $p = 1$ indicates no decay, while smaller values indicate faster decay of the activation energy at longer distances.

During the thermal activation stage, the time required for dislocations to overcome barriers is primarily determined by the waiting time of t_{w}. According to Orowan's law ($\gamma = N_{\text{m}} b \cdot \Delta l$), the equivalent true strain rate can be expressed as follows:

$$\dot{\varepsilon} = \frac{N_{\text{m}} b \cdot \Delta l}{M t_{\text{w}}} = \frac{N_{\text{m}} b \Delta l \nu_0}{M} \left[\exp\left(\frac{\Delta G}{k_B T} \right) - 1 \right]^{-1} \tag{4}$$

where, Δl represents the average distance traveled by dislocations between barriers, N_{m} denotes the mobile dislocation density. In the high strain rate regime, the mobile dislocation density dominates the total dislocation density, that is $N_{\text{m}} \approx N_{\text{tot}}$ [2,24]. M is the Taylor factor, where $\sigma = M\tau$, $\varepsilon = \gamma / M$, τ and γ represent the shear stress and strain, respectively. The reference strain rate is defined as $\dot{\varepsilon}_0 = N_{\text{m}} b \Delta l \nu_0 / M$ with general order of 10^7 s^{-1} [10]。

By substituting Eq.(4) into Eq.(3), and considering the relationship of $\Phi(\dot{\varepsilon}, T) = \sigma_{\text{th}} / \hat{\sigma}_{\text{th}}$, the following expression is obtained:

$$\Phi(\dot{\varepsilon}, T) = \left\{ 1 - \left[\frac{k_B T}{G_0} \ln\left(\frac{\dot{\varepsilon}_0}{\dot{\varepsilon}} + 1 \right) \right]^{1/q} \right\}^{1/p} \tag{5}$$

when the temperature exceeds the critical temperature T_{cr}, the thermal activation stress term disappears, and the flow stress is solely determined by the athermal stress component, that is $\sigma = \sigma_{\text{ath}}$. The expression for the critical temperature is given by:

$$T_{\text{cr}} = \left[\frac{k_B}{G_0} \ln\left(\frac{\dot{\varepsilon}_0}{\dot{\varepsilon}} + 1 \right) \right]^{-1} \tag{6}$$

2.1.2. Microstructural evolution

Based on the analysis of microstructural evolution in deformation processing experiments, one of the key features of metal deformation is the variation of cell size with strain. Sevillano's experimental results demonstrate that the cell size decreases with increasing equivalent plastic strain. For certain metals, the ratio of the average cell size δ to its saturated size δ_s is a function of equivalent plastic strain, and the data points cluster around a curve that is independent of the metal type [26]. The normalized cell size $\tilde{\delta}$, defined as the ratio of the average cell size to its initial value δ_0 ($\tilde{\delta} = \delta / \delta_0 \le 1$), can be described by the following evolution equation:

$$\frac{\mathrm{d}\tilde{\delta}}{\mathrm{d}\varepsilon} = -\frac{\delta_r}{\tilde{\delta}_s} \left[\tilde{\delta}^2 - \tilde{\delta}_s \tilde{\delta} \right] \tag{7}$$

Preprints (www.preprints.org) | NOT PEER-REVIEWED | Posted: 13 September 2023 doi:10.20944/preprints202309.0828.v1

where, δ_r is a dimensionless coefficient that represents the rate of cell refinement, while $\tilde{\delta}_s$ denotes the normalized saturated cell size (=δ_s/δ_0). Both are functions related to strain rate and temperature. It is worth noting that this study is consistent with the theoretical framework proposed by Molinari and Ravichandran [20], which suggests that δ is a generalized characteristic length of the microstructure and does not have a direct relationship with geometric dimensions. Therefore, the use of dimensionless size $\tilde{\delta}$ captures the essential trends in simulating microstructural evolution, where specific cell sizes of δ, δ_0, and δ_s become less important, and there is no need to precisely capture quantitative results regarding the microstructure.

The integral Eq.(7) yields the normalized cell size $\tilde{\delta}$, denoted as:

$$\tilde{\delta} = \frac{\tilde{\delta}_s}{1-\left(1-\tilde{\delta}_s\right)\exp\left(-\delta_r \varepsilon\right)} \tag{8}$$

The coefficients $\tilde{\delta}_s$ and δ_r can be expressed using the following empirical relationships [16]:

$$\begin{aligned} \tilde{\delta}_s &= \tilde{\delta}_{s0}\left[1-a_s\left(\frac{\dot{\varepsilon}}{\dot{\varepsilon}_r}\right)^{\xi_s}\cdot\max\left(\frac{T}{T_r},1\right)^{-\nu_s}\right] \\ \delta_r &= \delta_{r0}\left[1+a_r\left(\frac{\dot{\varepsilon}}{\dot{\varepsilon}_r}\right)^{\xi_r}\cdot\max\left(\frac{T}{T_r},1\right)^{-\nu_r}\right], \quad (\dot{\varepsilon}<\dot{\varepsilon}_r) \end{aligned} \tag{9}$$

where, T_r and $\dot{\varepsilon}_r$ represent the reference temperature and strain rate, respectively. a_s and a_r are non-negative constants, and ξ_s, ν_s, ξ_r, ν_r are constant values ranging from 0 to 1, controlling the dependence of $\tilde{\delta}_s$ and δ_r on strain rate and temperature. $\tilde{\delta}_{s0}$ represents the maximum reference saturated cell size δ_{s0} in comparison to its initial size ($\tilde{\delta}_s \le \tilde{\delta}_{s0} < 1$), while δ_{r0} is the minimum reference refinement rate ($\delta_{r0} \le \delta_r$). The normalized saturated cell size $\tilde{\delta}_s$ decreases with increasing deformation rate and increases with elevated temperature. Conversely, the cell refinement rate δ_r accelerates with higher deformation rates and decelerates with increasing temperature. The evolution of these two parameters indicates that under low-temperature and high-strain-rate conditions, the dynamic cell refinement rate is faster, resulting in smaller achievable saturated sizes. In Eq.(9), a modification is made to the temperature term, suggesting that the evolution of cell size becomes insensitive to temperature when it is lower than T_r.

Staker and Holt proposed a simple relationship between the average cell size δ and the average total dislocation density N_{tot}, which can be expressed as follows:

$$\delta = \frac{K_c}{\sqrt{N_{\text{tot}}}} \tag{10}$$

where, K_c is a material constant, with a value of 16 for OFHC.

Therefore, the square root of the normalized dislocation density is inversely proportional to the normalized cell size $\tilde{\delta}$:

$$\sqrt{\frac{N_{\text{tot}}}{N_0}} = \frac{1}{\tilde{\delta}} \tag{11}$$

By substituting the saturation value into equation (11), the normalized initial saturated cell size $\tilde{\delta}_{s0} = \sqrt{N_0/N_{s0}}$ can be obtained, where N_{s0} represents the minimum reference value (~ 10^{14} m^{-2} [28]) of the saturated dislocation density.

Preprints (www.preprints.org) | NOT PEER-REVIEWED | Posted: 13 September 2023 doi:10.20944/preprints202309.0828.v1

2.1.3. Threshold stress and thermal stress

In the theory of MTS, the threshold stress associated with thermal activation is related to microstructural evolution and can be expressed in combination with Eq.(11) as:

$$\hat{\sigma}_{\mathrm{th}} = M\hat{\alpha}\mu(T)b\sqrt{N_{\mathrm{tot}}} = \frac{\mu(T)}{\mu_0}\frac{1}{\tilde{\delta}}\cdot\left(M\hat{\alpha}\mu_0 b\sqrt{N_0}\right) \tag{12}$$

where, $\hat{\alpha}$ represents the intensity of dislocation interaction (< 1), and $\mu(T)$ is the temperature-dependent shear modulus. $\hat{\sigma}_0 = M\hat{\alpha}\mu_0 b\sqrt{N_0}$ represents a constant threshold stress value associated with the initial microstructure state at 0 K.

By substituting Eq.(8) into Eq.(12) and combining it with Eq.(5), the thermal activation stress can be expressed as:

$$\sigma_{\mathrm{th}} = \frac{\tilde{\mu}}{\tilde{\delta}_s}\hat{\sigma}_0\left[1-\left(1-\tilde{\delta}_s\right)\exp\left(-\delta_r\varepsilon\right)\right]\left\{1-\left[\frac{k_B T}{G_0}\ln\left(\frac{\dot{\varepsilon}_0}{\dot{\varepsilon}}+1\right)\right]^{1/q}\right\}^{1/p} \tag{13}$$

here, $\tilde{\mu}$ is the normalized shear modulus (= $\mu(T)/\mu_0$). The thermal activation stress consists of two components: the structural evolution (threshold stress) part and the strain rate and temperature response of the material under fixed structure. The structural evolution (normalized cell size) is related to strain rate and temperature. Therefore, the strain rate sensitivity of the thermal activation stress can be divided into two parts: the rate sensitivity of material strain hardening caused by structural evolution and the instantaneous rate sensitivity of stress [12,29].

Eq.(13) can also be written in the standard Voce-Kocks format [30]:

$$\sigma_{\mathrm{th}} = \sigma_{\mathrm{th}}^{\varepsilon=\infty} - \left(\sigma_{\mathrm{th}}^{\varepsilon=\infty} - \sigma_{\mathrm{th}}^{\varepsilon=0}\right)\exp\left(-\delta_r\varepsilon\right) \tag{14}$$

where, $\sigma_{\mathrm{th}}^{\varepsilon=\infty}$ and $\sigma_{\mathrm{th}}^{\varepsilon=0}$ represent the saturation and initial thermal activation stresses, respectively, with the following dependencies on strain rate and temperature:

$$\sigma_{\mathrm{th}}^{\varepsilon=0} = \tilde{\mu}\hat{\sigma}_0\Phi\left(\dot{\varepsilon},T\right), \quad \sigma_{\mathrm{th}}^{\varepsilon=\infty} = \sigma_{\mathrm{th}}^{\varepsilon=0}\tilde{\delta}_s^{-1} \tag{15}$$

2.2. Athermal stress

The athermal stress is a result of the interaction between dislocations and long-range obstacles, known as the Hall-Petch strengthening effect [12]. The long-range obstacles mainly include thermally independent grain boundaries and far-field forest dislocations. As the grain size decreases (~ μm), the number of grain boundaries increases, or the density of far-field forest dislocations increases with increasing deformation. These long-range obstacles hinder dislocation motion and capture more dislocations, thereby enhancing the material strength [31,32].

The Hall-Petch strengthening effect caused by the grain size effect can be expressed as follows [32,33]:

$$\sigma_{\mathrm{G}} = \sigma_0 + k_s D_0^{-1/2} \tag{16}$$

where, σ_0 represents the friction stress required for the motion of dislocations, which is typically negligible for FCC metals. k_s is the strengthening coefficient, and D_0 is the initial grain size.

The density of far-field forest dislocations N_f can be calculated using the rate-independent dislocation density evolution equation proposed by Klepaczko [12], where the effective forest dislocation density $\bar{N}_f$ is represented as:

Preprints (www.preprints.org) | NOT PEER-REVIEWED | Posted: 13 September 2023 doi:10.20944/preprints202309.0828.v1

$$\bar{N}_f = N_f - N_{f0} = \frac{M_{\mathrm{II}}}{k_{a0}}\left[1-\exp\left(-k_{a0}\varepsilon\right)\right] \tag{17}$$

where, M_{II} and k_{a0} are constants representing the proliferation rate and annihilation rate of dislocations, respectively. As the strain increases, the effective dislocation density approaches a saturation value, which is $\bar{N}_{fs} = M_{\mathrm{II}}/k_{a0}$.

The athermal stress can be expressed as [1,29]:

$$\sigma_{\mathrm{ath}} = \sigma_{\mathrm{G}} + \alpha_d \mu b\sqrt{\bar{N}_f} = \sigma_0 + k_s D_0^{-1/2} + \tilde{\mu} B\sqrt{1-\exp\left(-k_{a0}\varepsilon\right)} \tag{18}$$

here, *B* represents the stress at the saturation dislocation density at 0 K, denoted as $B = \alpha_d \mu_0 b\sqrt{\bar{N}_{fs}}$, and α_d is a material constant (< 1). The athermal stress indirectly achieves the thermal softening effect of the material through the relationship between the shear modulus (elastic field) and temperature. It realizes strain hardening of the material through the generation and storage of dislocations during deformation, while the deformation rate does not affect the evolution of non-thermal stress.

2.3. Flow stress and hardening rate

Finally, combining Eq.(13) and Eq.(18), the constitutive relationship for the flow stress of FCC metals is obtained as:

$$\begin{aligned}\sigma &= \sigma_0 + k_s D_0^{-1/2} + \tilde{\mu} B\sqrt{1-\exp\left(-k_{a0}\varepsilon\right)} \\ &+ \tilde{\mu}\frac{\hat{\sigma}_0}{\tilde{\delta}_s}\left[1-\left(1-\tilde{\delta}_s\right)\exp\left(-\delta_r\varepsilon\right)\right]\left\{1-\left[\frac{k_B T}{G_0}\ln\left(\frac{\dot{\varepsilon}_0}{\dot{\varepsilon}}+1\right)\right]^{1/q}\right\}^{1/p}\end{aligned} \tag{19}$$

The strain hardening rate with respect to stress is given by:

$$\frac{\mathrm{d}\sigma}{\mathrm{d}\varepsilon} = \frac{\mathrm{d}\sigma_{\mathrm{ath}}}{\mathrm{d}\varepsilon} + \frac{\mathrm{d}\sigma_{\mathrm{th}}}{\mathrm{d}\varepsilon} = \frac{k_{a0}}{2}\left[\frac{\left(\sigma_{\mathrm{ath}}^{\varepsilon=\infty} - \sigma_G\right)^2}{\sigma_{\mathrm{ath}} - \sigma_{\mathrm{G}}} - \left(\sigma_{\mathrm{ath}} - \sigma_{\mathrm{G}}\right)\right] + \delta_r\left(\sigma_{\mathrm{th}}^{\varepsilon=\infty} - \sigma_{\mathrm{th}}\right) \tag{20}$$

where, the first term represents the strain hardening rate induced by the evolution of long-range obstacles in the microstructure, such as grain size and grain boundaries. The hardening rate initially decreases inversely proportional to the athermal stress and follows a linear function with a constant slope k_{a0} at higher stresses. The second term accounts for the strain hardening rate due to thermal stress arising from the evolution of short-range obstacles, such as line defects represented by dislocation spacing. Under stable loading conditions, the hardening rate decreases linearly as the thermal stress increases, where δ_r is a constant.

Observing the model's behavior under constant loading conditions (stable strain rate and temperature), the overall strain hardening rate exhibits a rapid decrease as the deformation intensifies due to the inverse proportional function, reflecting the hardening characteristics of FCC metals at stage III [11,26]. Once the material reaches a certain level of strengthening, the overall strain hardening rate gradually decreases linearly until it approaches zero, with a slope approximately equal to $-\left(k_{a0}+\delta_r\right)$. This behavior is consistent with the hardening characteristics of stage IV [26,34]. Since k_{a0} is a material constant, the sensitivity of the hardening rate to strain rate and temperature primarily depends on the microstructural refinement rate δ_r .

2.4. Shear modulus

Preprints (www.preprints.org) | NOT PEER-REVIEWED | Posted: 13 September 2023 doi:10.20944/preprints202309.0828.v1

The Nadal-Le Poac (NP) shear modulus model replaces the empirical temperature dependence of the shear modulus in the SCG model with an equation based on the Lindemann melting theory. This modification enhances the robustness of the model when applied under high-temperature and high-pressure conditions. Moreover, the NP model mitigates the instantaneous decrease of the shear modulus at the melting point. The zero-pressure form of the NP shear modulus model can be expressed as:

$$\mu(T)=\frac{1}{\Gamma(T/T_m)}\left[\mu_0\left(1-\frac{T}{T_m}\right)+\frac{\rho_{\mathrm{m}}}{\tilde{C}m_u}k_BT\right]$$
$$\Gamma(T/T_m)=1+\exp\left[-\frac{1+1/\zeta_{\mathrm{m}}}{1+\zeta_{\mathrm{m}}/(1-T/T_m)}\right] \tag{21}$$

where, ρ_{m} represents the material's standard density, T_m denotes the melting point of the material under standard conditions, $\tilde{C}$ is a material constant related to the Lindemann constant, m_u signifies the atomic mass, $\Gamma(T/T_m)$ controls its nonlinear behavior when $T/T_m \approx 1$, and $\zeta_{\mathrm{m}} \ll 1$ serves as a fitting parameter that governs the overall fit quality.

2.5. Adiabatic temperature rise

During metal deformation process, experimentally found that the majority of the energy supplied to effect plastic deformation converted to heat, contributing to an increase in temperature [36,37]. The conversion coefficient β generally falls within the range of 0.9 to 1.0 for high deformation rates (> 1 s^{-1}) in adiabatic processes [37,38]. If adiabatic shear banding (ASB) occurs under high strain rates, the heat generated during plastic deformation can lead to a rapid increase in temperature within the localized region of the adiabatic shear band. The equation connecting temperature raising and plastic work is presented in an integral format [39]:

$$T=T_0+\frac{\beta}{\rho_{\mathrm{m}}C_p}\int_0^{\varepsilon}\sigma(\varepsilon,\dot{\varepsilon},T)d\varepsilon \tag{22}$$

where, T_0 is the initial temperature, C_p is the specific heat of the material at constant pressure. In the calculation of flow stress during adiabatic processes, it is necessary to update the temperature state variable at each incremental strain step.

3. Application

This section presents the material parameters used in the model for annealed OFHC and compares the predicted results with experimental data. The results cover the influence of strain rate on flow stress under fixed strains, as well as the deformation behavior of annealed OFHC across a wide range of strain rates (4×10^{-4} to 6.4×10^{5} s^{-1}) at room temperature, and a broad temperature range (77 to 1096 K) at a strain rate of 4000 s^{-1}.

3.1. Parameter calibration

The physical constants of annealed OFHC and the parameters in the NP shear modulus model at zero hydrostatic pressure are shown in Table 1.

Table 1. Parameters in the NP shear modulus model and temperature evolution model of OFHC.

ρ_{m} (kg/m³)	C_p (J/kg/K)	β	μ_0 (GPa)	T_{m} (K)	ζ_{m}	$\tilde{C}$	m_u (amu)
8930	382	0.9	50.7	1356	0.04	0.057	63.55

In the component of athermal stress, Meyers et al. conducted a study and found that the value of k_s for OFHC decreases linearly with increasing strain under low strain rates, ranging from (56 −

Preprints (www.preprints.org) | NOT PEER-REVIEWED | Posted: 13 September 2023 doi:10.20944/preprints202309.0828.v1

260) MPa $\sqrt{\mu m}$. However, at high strain rates, the value remains approximately constant. This behavior is taken into account in the ZA model [14], where an intermediate value is employed. The coefficients for the athermal stress in the model are provided in Table 2.

Table 2. Material coefficients in the athermal stress component.

σ_G (MPa)	k_s (MPa $\sqrt{\mu m}$)	D_0 (μm)	B (MPa)	k_{a0}
20.6	158 [14]	62	230 [2]	0.64 [2]

The material parameters for the thermal stress component are described in the following two tables. Table 3 provides the parameters that are independent of microstructural evolution, calculated $\hat{\sigma}_0$ as 50.2 MPa based on the data.

Table 3. Material parameters in the thermal stress component that are independent of microstructure.

N_0 (m^{-2})	M	$\hat{\alpha}$	b (nm)	k_B/G_0 (K^{-1})	p	q	$\dot{\varepsilon}_0$ (s^{-1})
10^{13} [39]	3.06 [40]	0.4 [41]	0.256 [26]	4.9×10^{-5} [15]	2/3 [10]	1 [10]	10^7 [10]

The parameters for the normalized cell size evolution model are proposed by Molinari and Ravichandran and illustrated in Table 4. By utilizing the data in the table and Eq.(11), the minimum value of the reference saturated dislocation density is approximately 7×10^{14} m^{-2}, which consistent with the actual physical laws.

Table 4. Parameters of the evolution equation for normalized cell size.

$\tilde{\delta}_{s0}$	a_s	ξ_s	v_s	δ_{r0}	a_r	ξ_r	v_r	$\dot{\varepsilon}_r$ (s^{-1})	T_r (K)
0.12	0.377	0.24	0.5	4.3	50	0.8	0	10^7	298

3.2. Simulation results

The experimental values for comparison with the model calculations can be found in Appendix A. In Fig. 1, the relationships between flow stress, normalized cell size, and strain rate for OFHC at fixed strains and room temperature are depicted. It is noteworthy that the sensitivity of flow stress to strain rate undergoes a sudden change at 10^4 s^{-1}, which aligns with the evolution pattern of the normalized reciprocal cell size $\tilde{\delta}^{-1}$. This observation suggests that the sensitivity of flow stress to strain rate is dominated by the microstructural evolution law. Specifically, when $\dot{\varepsilon}$ <10^4 s^{-1}, the normalized reciprocal cell size lines are horizontally parallel with fixed strains. This behavior arises from the fact that the saturation size and refinement rate, as controlled by Eq.(9), remain approximately constant, indicating that the microstructure exhibits low sensitivity to changes in strain rate. Additionally, the sensitivity of flow stress to strain rate is influenced by the term $\Phi(\dot{\varepsilon},T)$. At extremely low strain rates ($\dot{\varepsilon}$ <10^{-3} s^{-1}), the value of $\Phi(\dot{\varepsilon},T)$ exhibits minimal variation with strain rate, implying that the flow stress is predominantly determined by the deformation level and temperature.

Preprints (www.preprints.org) | NOT PEER-REVIEWED | Posted: 13 September 2023 doi:10.20944/preprints202309.0828.v1

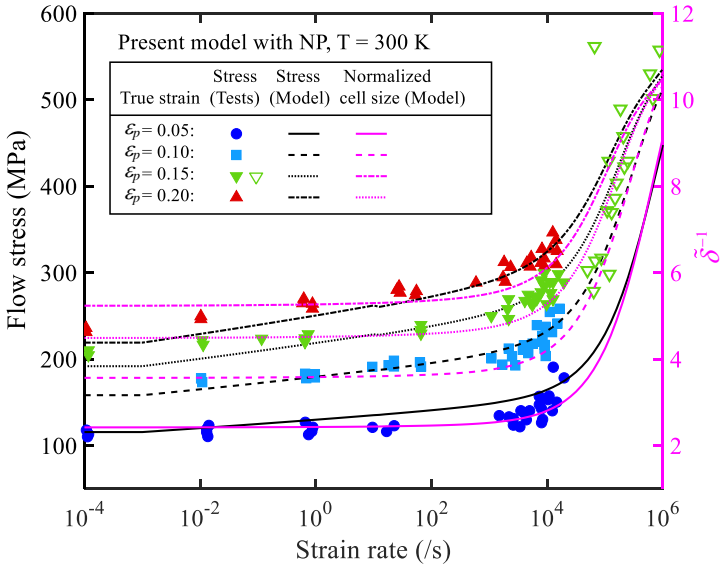

Figure 1. Relationship between flow Stress, normalized cell size, and strain rate of annealed OFHC at fixed strain and room temperature.

Fig. 2 and Fig. 3 present the relationship between flow stress and strain within a wide range of strain rates at room temperature and a wide range of temperatures at a fixed strain rate for OFHC, respectively. The results demonstrate a strong agreement between the model's predicted values and the experimental data, which will be further analyzed in the subsequent section to quantify the error. In Fig. 2, when the strain exceeds ε_1 (≈ 0.2), a distinct change in the surface occurs near 1 s^{-1} for a fixed strain. Within a narrow range of strain rates, an intriguing phenomenon emerges as the flow stress decreases with increasing strain rate. This intriguing behavior can be attributed to the consideration of temperature increase induced by plastic deformation when $\dot{\varepsilon} > 1$ s^{-1}, where the thermal softening effect of the material surpasses the strengthening effect associated with strain rate.

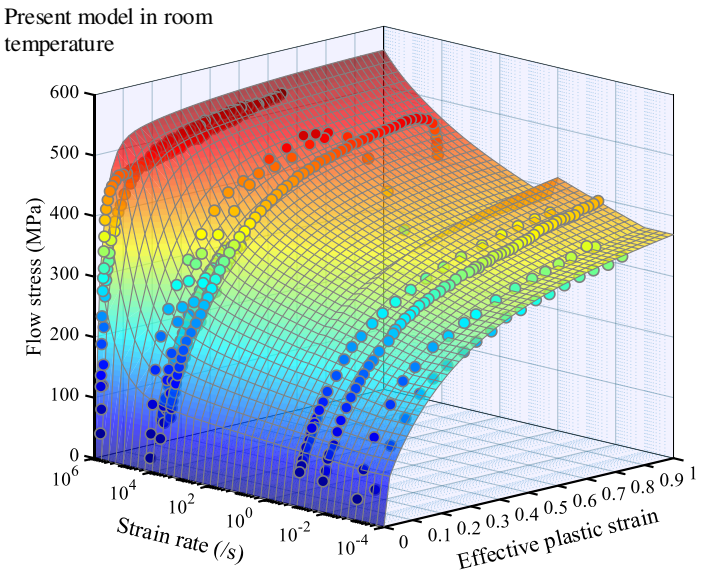

Figure 2. Flow stress-strain curved surface of annealed OFHC over a wide strain rate range at room temperature.

Preprints (www.preprints.org) | NOT PEER-REVIEWED | Posted: 13 September 2023 doi:10.20944/preprints202309.0828.v1

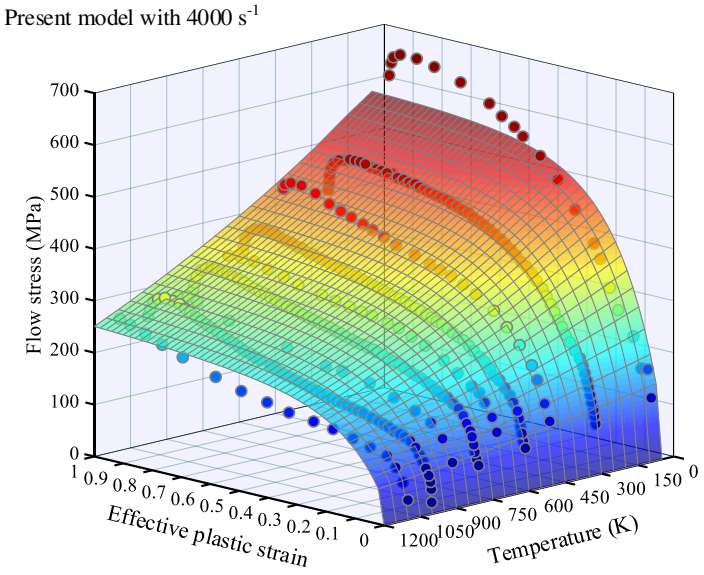

Figure 3. Flow stress-strain curved surface of annealed OFHC over a wide temperature range with $\dot{\varepsilon} = 4000\ s^{-1}$.

4. Result analysis and discussion

4.1. Relative error analysis

Based on the experimental results of OFHC across a wide range of strain rates and deformation temperatures, Biswajit Banerjee conducted a meticulous evaluation in their research [42,43]. They identified the hierarchical order of the model's evaluation errors: PTW, MTS, ZA, JC, SCGL (Steinberg-Cochran-Guinan-Lund [44]). Notably, the present model's microstructure evolution is predicated upon the MR model, while the validation experiments predominantly stem from Nemat-Nasser and Li [15]. To enhance the understanding of the predictive accuracy of the constitutive models, the paper undertakes a thorough analysis of errors and evaluated the performance of not only the present model but also five alternative constitutive models: MTS, PTW, JC, NNL, and MR. This comprehensive assessment encompassed a total of six distinct models, providing valuable insights into their respective prediction capabilities.

The relative error values $E_{i,j}$ are computed using Eq.(23):

$$E_{i,j}(\%) = \frac{\sigma_{i,j}^{\mathrm{pre}} - \sigma_{i,j}^{\mathrm{exp}}}{\sigma_{i,j}^{\mathrm{exp}}} \times 100\% \tag{23}$$

where, $\sigma_{i,j}^{\mathrm{pre}}$ denotes the model-predicted flow stress and $\sigma_{i,j}^{\mathrm{exp}}$ represents the experimental flow stress. The subscripts '*i*' and '*j*' signify the relative error for the *i*-th data point under the *j*-th deformation condition.

Fig. 4 and Fig. 5 showcase the error curves representing the disparities between the predicted flow stress of OFHC using six distinct models and the corresponding experimental results. The order in which these models are presented is as follows: (a) Present, (b) MTS, (c) NNL, (d) PTW, (e) JC, and (d) MR. Models (a) to (d) encompass constitutive models that incorporate microstructure evolution, while model (e) is an empirical model and (f) is a semi-empirical physical model.

As shown in Fig. 4(a), the present model exhibits relatively larger relative errors (between ±20%) in predicting results at room temperature and strain rates of 8000 s^{-1} and 13000 s^{-1}. However, under other strain rate conditions, the relative errors of the model are mainly within ±10%. Notably, the relative error curves of the other five models at the above two strain rates exhibit similar trends to that of the present model. Therefore, it is plausible that these significant discrepancies may stem from

Preprints (www.preprints.org) | NOT PEER-REVIEWED | Posted: 13 September 2023 doi:10.20944/preprints202309.0828.v1

experimental errors at these two strain rates. Regarding extremely high strain rates (6.4×10^5 s^{-1}), the present model, PTW, and MR demonstrate relatively accurate prediction results, while the MTS model exhibits a slightly higher values compared to the present. Both NNL and JC models significantly underestimate the experimental results at low strains, with relative errors approaching -40%. Nevertheless, the accuracy of NNL predictions notably improves as the strain increases, while the JC model still remains approximately -20%. Moreover, under all other strain rate conditions, the JC model overestimates material flow stress at low strains with relative errors exceeding +20%. Excluding the JC model, the other models exhibit satisfactory consistency with the experimental results across the range of 0.001 − 8500 s^{-1}. However, at an extremely low strain rate of 4×10^{-4} s^{-1}, all models predict higher values than the experimental results. Generally speaking, the predictions of the present model outperform those of the other models. This discrepancy can be attributed to the fact that the dislocation slip velocity is slower at relatively low strain rates, resulting in prolonged interaction time between dislocations and internal defects or barriers within the material. Consequently, dislocation diffusion or dispersion mechanisms may become the dominant deformation mechanisms, leading to a decrease in material strength and causing the model to predict higher flow stress values compared to the experimental data [45,14].

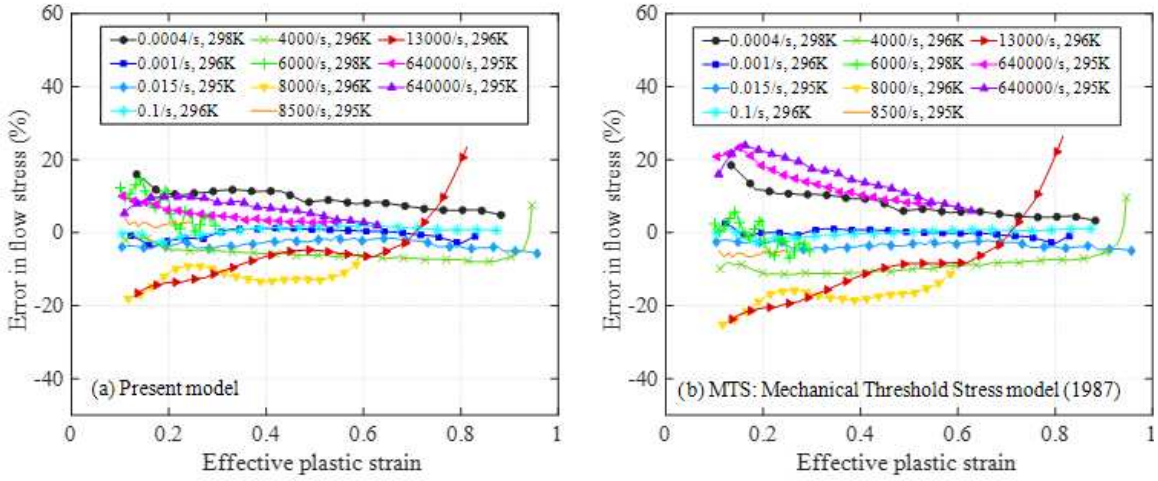

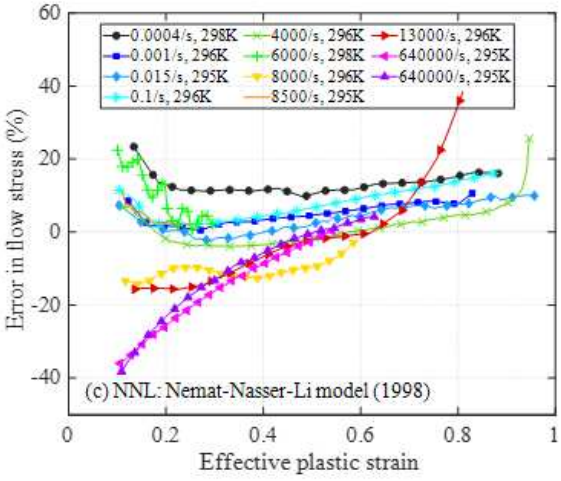

Preprints (www.preprints.org) | NOT PEER-REVIEWED | Posted: 13 September 2023 doi:10.20944/preprints202309.0828.v1

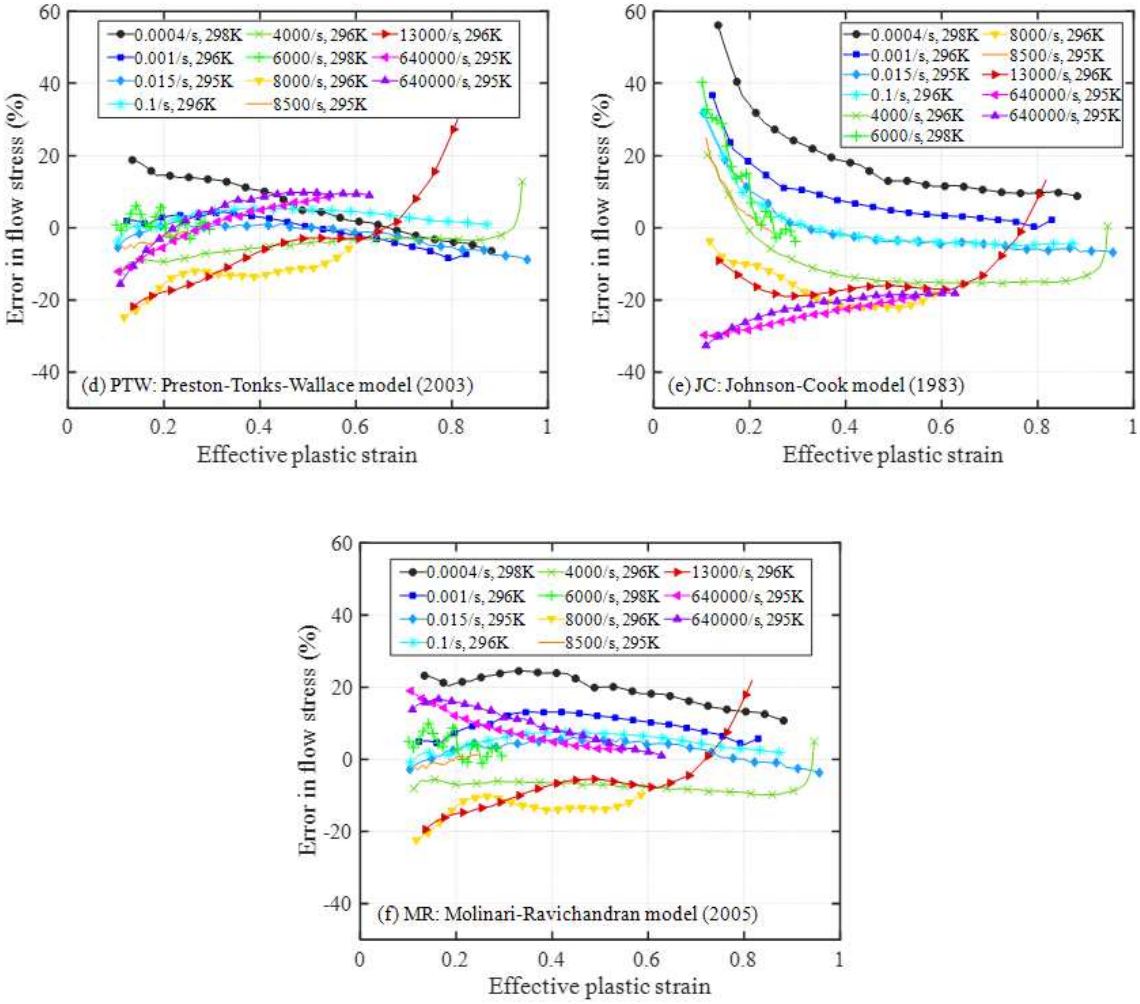

Figure 4. The relative error curve between the predicted values of models and the experimental results over a wide range of strain rates at room temperature.

The relative error curves of Fig. 5 (a), (b), and (f) exhibit a high degree of similarity. These error curves demonstrate a consistent pattern, where the curves gradually shift upwards as the temperature increases, indicating that the predicted values are higher compared to the experimental results at high temperatures. Furthermore, for model (c) NNL, its predicted values are consistently higher than the experimental values at both high and low temperatures. This behavior can be attributed to the fact that, under high-temperature, the solid-state diffusion rate in the crystal significantly increases, promoting grain growth. Larger grains may contain more structural defects or dislocations, resulting in a decrease in material strength. Since these models does not account for microstructural coarsening, the predicted results at high temperatures tend to be higher than the experimental ones. On the other hand, PTW and JC models underestimate the material's flow stress at higher temperatures, and as the strain increases, their predictions deviate even further from the experimental results. From the perspective of the error curves, the MTS model exhibits the best predictive performance, while there is still room for improvement in the present model's predictions at higher temperatures (> 0.7 T_m).

Preprints (www.preprints.org) | NOT PEER-REVIEWED | Posted: 13 September 2023 doi:10.20944/preprints202309.0828.v1

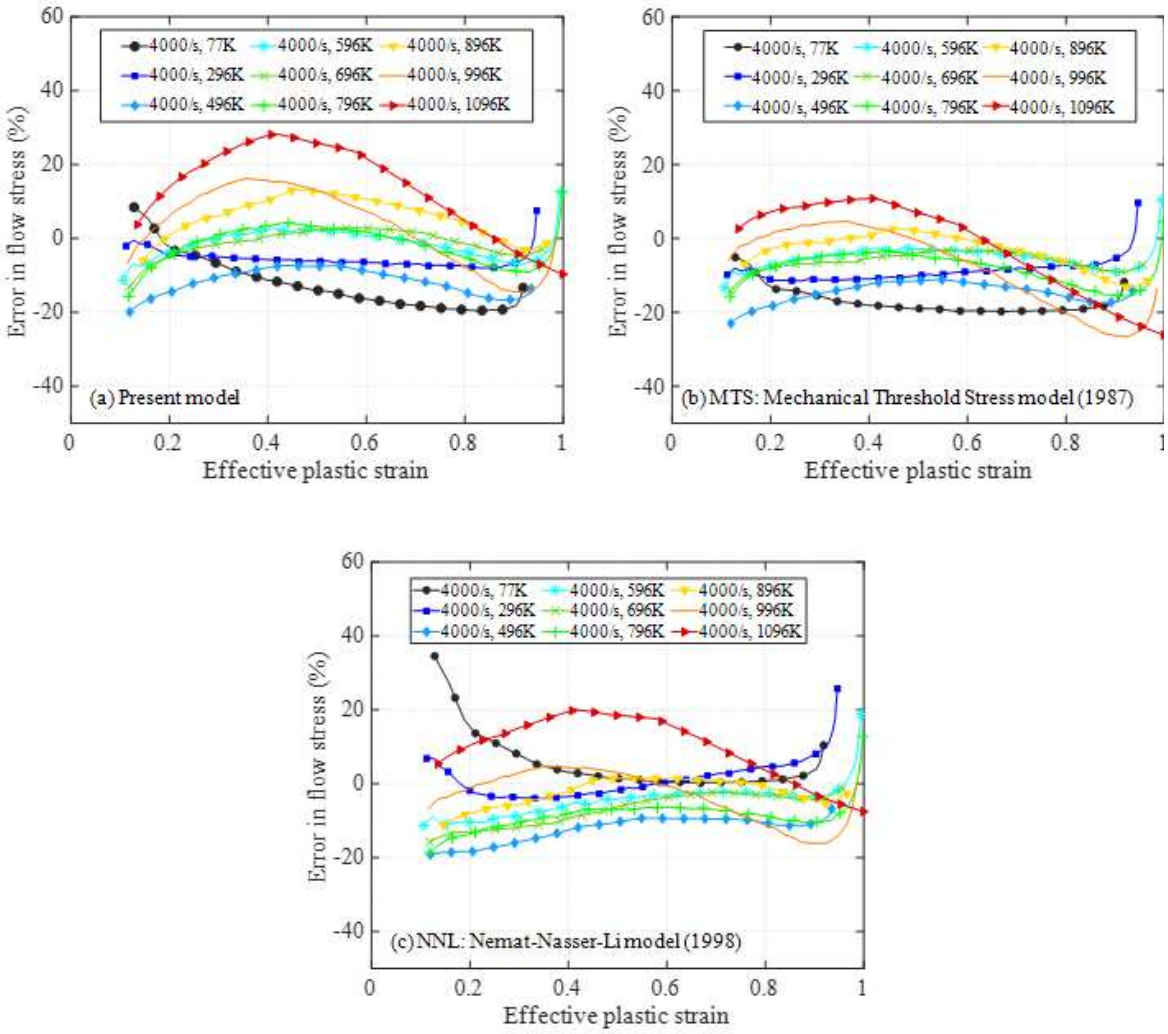

Preprints (www.preprints.org) | NOT PEER-REVIEWED | Posted: 13 September 2023 doi:10.20944/preprints202309.0828.v1

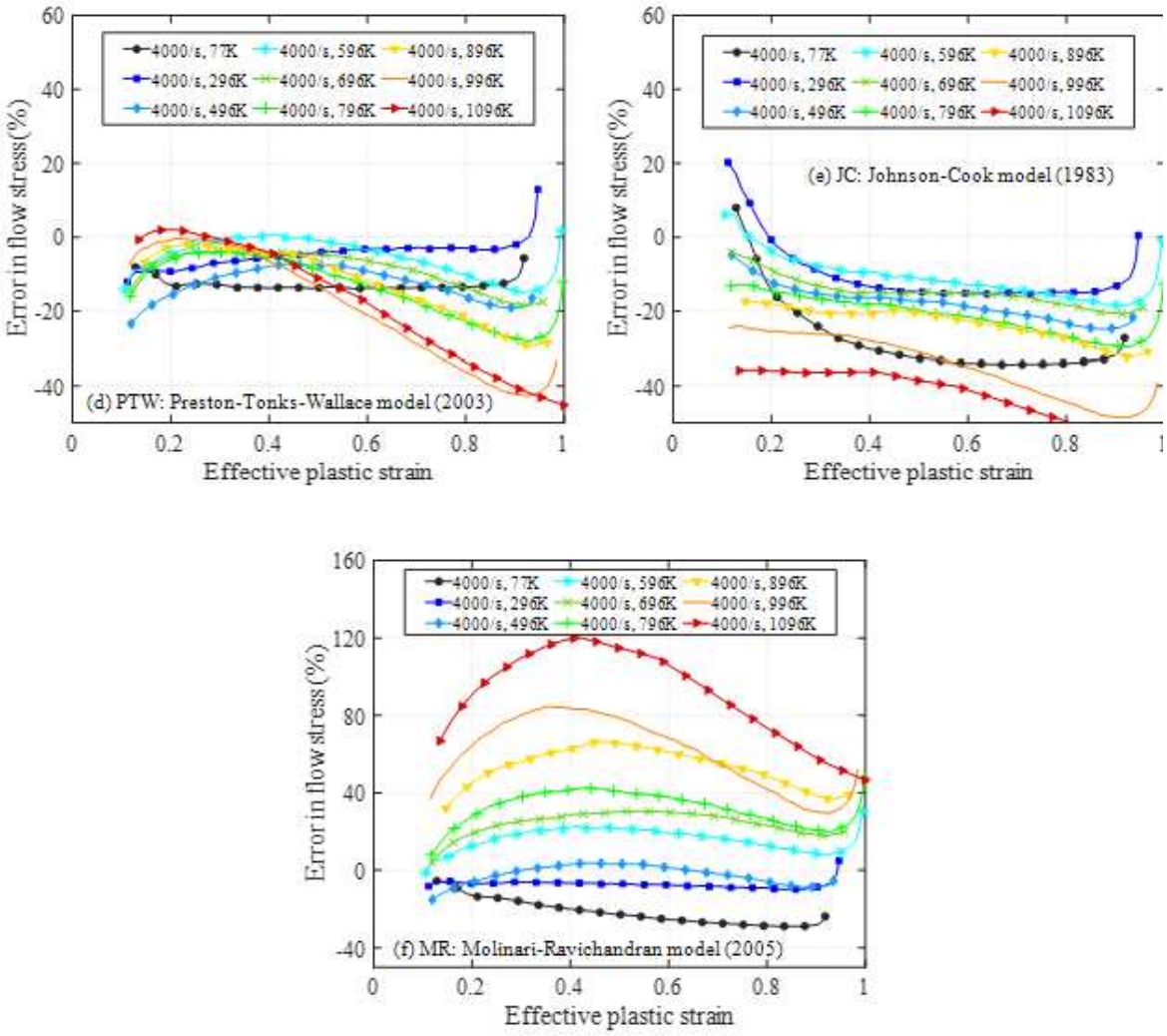

Figure 5. The relative error curve between the predicted values of models and the experimental results over a wide range of temperatures at strain rate of 4000 s^{-1}.

4.2. Comprehensive error analysis

To provide a more comprehensive assessment of the predictive capabilities of the abovementioned six constitutive models for the flow stress of OFHC, three statistical average errors were employed to evaluate the model predictions. These include the mean absolute relative error of plastic work (MARE-P.WK, $\bar{E}_{\mathrm{AR.W}}$), the mean absolute relative error of flow stress (MARE-F.S, $\bar{E}_{\mathrm{AR.Y}}$), and the mean maximum absolute error of flow stress (MMAE-F.S, $\bar{E}_{\mathrm{MA.Y}}$). The calculation formulas for these metrics are as follows:

$$\bar{E}_{\mathrm{AR.W}} = \frac{1}{J}\sum_{j=1}^{J}\frac{W_j^{\mathrm{pre}} - W_j^{\mathrm{exp}}}{W_j^{\mathrm{exp}}} \times 100\%, \quad W_j = \int_0^{\varepsilon} \sigma_j d\varepsilon \tag{24}$$

$$\bar{E}_{\mathrm{AR.Y}} = \frac{1}{J}\sum_{j=1}^{J}\left(\frac{1}{I_j}\sum_{i=1}^{I_j}\left|E_{i,j}\right|\right) \tag{25}$$

$$\bar{E}_{\mathrm{MA.Y}} = \frac{1}{J}\sum_{j=1}^{J}\left[\left|\bar{E}_j\right| + \sqrt{\frac{1}{I_j}\sum_{i=1}^{I_j}\left(E_{i,j} - \bar{E}_j\right)^2}\right], \quad \bar{E}_j = \frac{1}{I_j}\sum_{i=1}^{I_j}E_{i,j} \tag{26}$$

Preprints (www.preprints.org) | NOT PEER-REVIEWED | Posted: 13 September 2023 doi:10.20944/preprints202309.0828.v1

where, I_j represents the total number of data points with the deformation condition of index j, $\bar{E}_j$ denotes the average value of the relative error curve j. and J refers to the total number of experimental data that satisfy the statistical criteria. For example, there are four sets of experimental data with $\dot{\varepsilon} \leq 10^3$ s^{-1} at room temperature, that is $J = 4$.

The statistical average errors for the predictions of the six models under different strain rate gradients at room temperature are presented in Fig. 6. It is observed that the majority of the models perform well in accurately capturing the flow stress behavior of the material at low strain rates, with the exception of the JC model which exhibits a higher MMAE-F.S value. The strain rate sensitivity of the flow stress undergoes a notable transition within the range of 10^3 s^{-1} – 10^4 s^{-1}. Specifically, the present model, MTS, and NNL models exhibit relatively low statistical average errors of approximately 10% within this range, while the JC and MR models demonstrate larger errors exceeding >20%. This finding indicates that the abrupt change in flow stress sensitivity of OFHC is significantly influenced by microstructural evolution. Moreover, at extremely high strain rates, the values of MMAE-F.S for the MTS, NNL, and JC models exceed 20%, suggesting that these three models may not yield accurate results under such extreme high-strain-rate conditions.

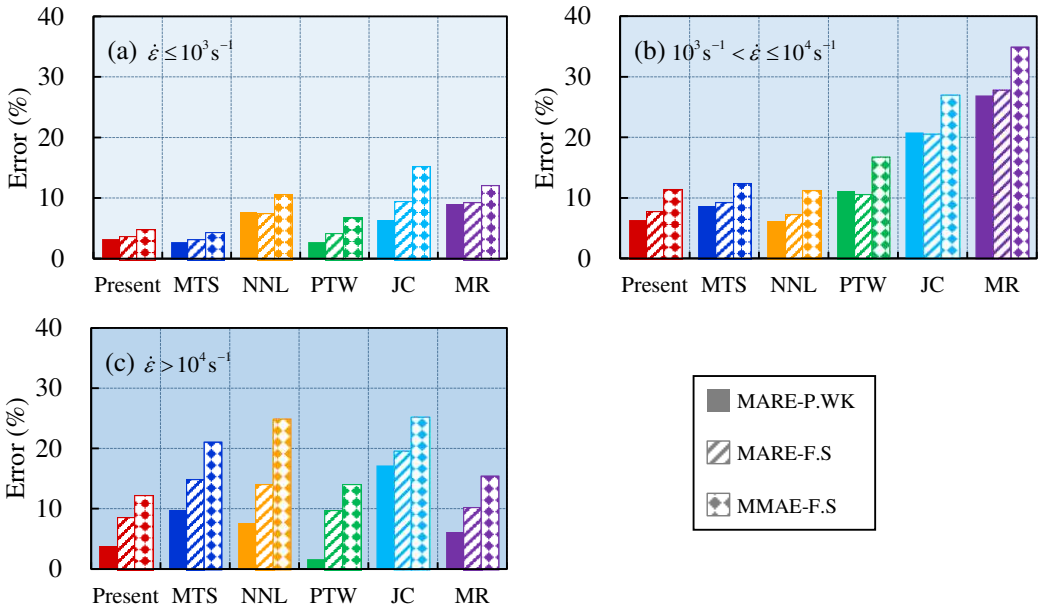

Figure 6. Three statistical average errors of model predictions within different strain rate ranges: MARE-P.WK, MARE-F.S, and MMAE-F.S.

The statistical average errors for the predictions of the six models under different temperature gradients at a strain rate of 4000 s^{-1} are shown in Fig. 7. It is observed that the present model, MTS, and NNL models consistently demonstrate relatively small statistical average errors across all temperature ranges (maximum value is approximately 10%). The PTW and MR models demonstrate statistical average errors below 10% at temperatures below 0.4 T_m. However, as the temperature increases, the statistical average errors increase as well. Notably, the MR model exhibits statistical average errors exceeding 20% within the intermediate temperature range and even surpass 60% at high temperatures. Therefore, the MR and PTW models are deemed unsuitable for high-temperature conditions. Moreover, throughout the entire temperature range, the JC model displays statistical average errors ranging from 15% to 30%. This indicates that the standard JC model is not suitable for simulations involving strain rates equal to or greater than 4000 s^{-1}.

Preprints (www.preprints.org) | NOT PEER-REVIEWED | Posted: 13 September 2023 doi:10.20944/preprints202309.0828.v1

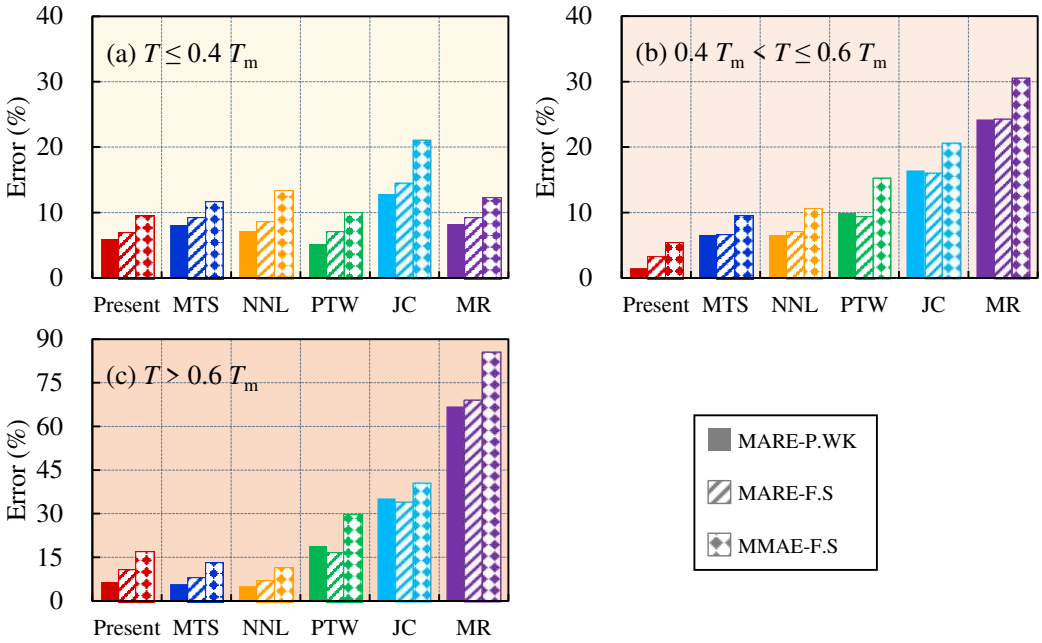

Figure 7. Three statistical average errors of model predictions within different temperature ranges: MARE-P.WK, MARE-F.S, and MMAE-F.S.

The statistical average errors in model predictions across all strain rates and temperature ranges are comprehensively evaluated and presented in Fig. 8. The enclosed triangle area formed by the lines serves as a measure of the model's prediction accuracy, with a smaller area indicating higher precision. When considering different strain rates, the sizes of the triangles formed by the three statistical average errors follow the order: Present ≈ PTW < MTS < MR < NNL < JC. Similarly, for varying temperatures, the triangle sizes adhere to the sequence: Present ≈ NNL < MTS < PTW < JC < MR. From the results, it is evident that the proposed model demonstrates favorable simulation outcomes across a broad range of strain rates and temperatures.

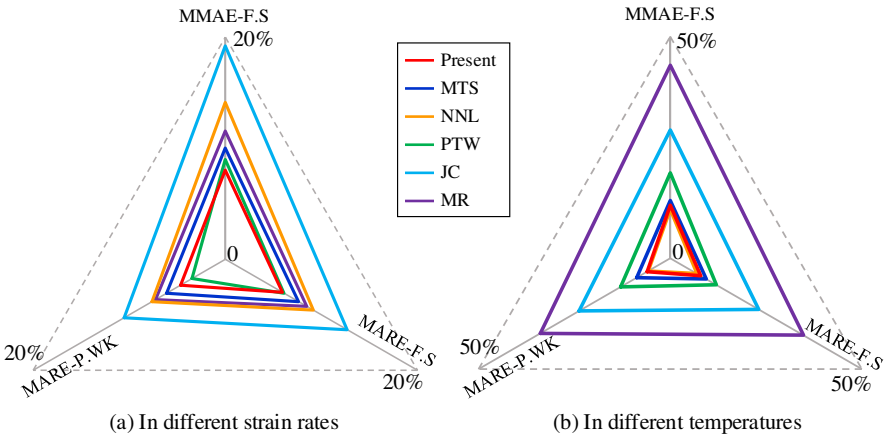

Figure 8. Comprehensive evaluation of three statistical average errors in model prediction results.

5. Conclusion

Based on a normalized cell size evolution model, coupled with the dislocation density evolution mechanism and the influence of dislocation motion on plastic deformation, a semi-empirical physical constitutive model was developed in this study. By capturing the sensitivity of microstructural evolution to strain rate, the model can successfully captures the sharp increase in flow stress at strain rates exceeding a critical value at fixed strain.

 doi:10.20944/preprints202309.0828.v1

The proposed model effectively describes the strain rate sensitivity transition of flow stress around 10^4 s^{-1} when applied to annealed OFHC. A comparison of the models' predictions with those of the MTS, NNL, PTW, JC, and MR models reveals that the microstructure-based constitutive model is more suitable for describing material plastic deformation behavior at high strain rates. The predictive capability of the proposed model outperforms other models across a wide range of strain rates (4×10^{-4} – 6.4×10^5 s^{-1}) and temperatures (77 – 1096 K). These research findings provide valuable guidance for selecting appropriate models in engineering applications and enhancing the understanding of the rheological behavior of OFHC. However, limitations still exist in the proposed model. High temperatures introduce complexities in the nonlinear mechanical behavior of materials, such as grain growth and the generation of structural defects, which require further investigation regarding their effects on plastic deformation and the influence of temperature on microstructural evolution.

Acknowledgments: The authors would like to acknowledge the China Scholarship Council, China (Grant No. 201906840011), and National Natural Science Foundation of China (Grant Nos. 11972196) for the financial support.

Appendix A. Source of experimental data

Table 1. Experimental results on the relationship between flow stress and strain rate of OFHC at fixed strain and room temperature.

Condition	ε	$\dot{\varepsilon}$ (s^{-1})	T (K)	References
Fixed strain.	0.15	$\dot{\varepsilon} \in 6\times(10^4, 10^5)$		[40,41] Tong and Clifton (1992, 1998)
Room temperature.	0.05, 0.10, 0.15, 0.20.	$\dot{\varepsilon} \in (10^{-4}, 2\times10^4)$	300	Preston, Tonks, and Wallace (2003)

Table 2. Experimental results on the flow stress-strain relationship of OFHC over a wide range of strain rates at room temperature.

Condition	$\dot{\varepsilon}$ (s^{-1})	T (K)	References
	0.015, 8500, 640000.	295	Follansbee and Kocks (1988)
Room temperature.	0.001, 0.1, 4000, 8000.	296	Nemat-Nasser and Li (1998)
Wide range of strain rates.	0.0004, 6000.	298	Tanner and McGinty (1999)
	13000	296	Jing and Wang (2022)

Table 3. Experimental results on the flow stress-strain relationship of OFHC over a wide range of temperatures at a fixed strain rate.

Condition	$\dot{\varepsilon}$ (s^{-1})	T (K)	References
Fixed strain rate.	4000	77, 296, 496, 596, 696,	Nemat-Nasser and Li (1998)
Wide range of temperatures.		796, 896, 996, 1096.	

Reference

1. Armstrong RW, Walley SM. High strain rate properties of metals and alloys. International Materials Reviews 2008;53:105–28. https://doi.org/10.1179/174328008X277795.
2. Gao CY, Zhang LC. Constitutive modelling of plasticity of fcc metals under extremely high strain rates. International Journal of Plasticity 2012;32–33:121–33. https://doi.org/10.1016/j.ijplas.2011.12.001.
3. Salvado F, Teixeira-Dias F, Walley SM, Lea L, Cardoso J. A review on the strain rate dependency of the dynamic viscoplastic response of FCC metals. Progress in Materials Science 2017;88. https://doi.org/10.1016/j.pmatsci.2017.04.004.
4. Jia X, Hao K, Luo Z, Fan Z. Plastic Deformation Behavior of Metal Materials: A Review of Constitutive Models. METALS 2022;12. https://doi.org/10.3390/met12122077.
5. Johnson GR, Cook WH. A constitutive model and data for materials subjected to large strains, Proceedings 7th International Symposium on Ballistics, The Hague: 1983, p. 541–7.
6. Rule WK, Jones SE. A revised form for the Johnson–Cook strength model. International Journal of Impact Engineering 1998;21:609–24. https://doi.org/10.1016/S0734-743X(97)00081-X.
7. Wang J, Guo W-G, Li P, Zhou P. Modified Johnson-Cook description of wide temperature and strain rate measurements made on a nickel-base superalloy. Materials at High Temperatures 2017;34:157–65. https://doi.org/10.1080/09603409.2016.1252164.
8. Wang Y, Zeng X, Chen H, Yang X, Wang F, Zeng L. Modified Johnson-Cook constitutive model of metallic materials under a wide range of temperatures and strain rates. Results in Physics 2021;27:104498. https://doi.org/10.1016/j.rinp.2021.104498.
9. Kumar Reddy Sirigiri V, Yadav Gudiga V, Shankar Gattu U, Suneesh G, Mohan Buddaraju K. A review on Johnson Cook material model. Materials Today: Proceedings 2022;62:3450–6. https://doi.org/10.1016/j.matpr.2022.04.279.
10. Follansbee PS, Kocks UF. A constitutive description of the deformation of copper based on the use of the mechanical threshold stress as an internal state variable. Acta Metallurgica 1988;36:81–93. https://doi.org/10.1016/0001-6160(88)90030-2.
11. Mecking H, Kocks UF. Kinetics of flow and strain-hardening. Acta Metallurgica 1981;29:1865–75. https://doi.org/10.1016/0001-6160(81)90112-7.
12. Klepaczko JR. Physical-state variables — the key to constitutive modeling in dynamic plasticity. Nuclear Engineering and Design 1991;127:103–15. https://doi.org/10.1016/0029-5493(91)90043-H.
13. Mohamadnejad S, Basti A, Ansari R. Analyses of Dislocation Effects on Plastic Deformation. Multiscale Sci Eng 2020;2:69–89. https://doi.org/10.1007/s42493-020-00037-2.
14. Zerilli FJ, Armstrong RW. Dislocation-mechanics-based constitutive relations for material dynamics calculations. Journal of Applied Physics 1987;61:1816–25. https://doi.org/10.1063/1.338024.
15. Nemat-Nasser S, Li Y. Flow stress of f.c.c. polycrystals with application to OFHC Cu. Acta Materialia 1998;46:565–77. https://doi.org/10.1016/S1359-6454(97)00230-9.
16. Gao CY, Zhang LC. A constitutive model for dynamic plasticity of FCC metals. Materials Science and Engineering: A 2010;527:3138–43. https://doi.org/10.1016/j.msea.2010.01.083.
17. Austin RA, McDowell D. A dislocation-based constitutive model for viscoplastic deformation of fcc metals at very high strain rates. International Journal of Plasticity 2011;27:1–24. https://doi.org/10.1016/j.ijplas.2010.03.002.
18. Austin RA, McDowell DL. Parameterization of a rate-dependent model of shock-induced plasticity for copper, nickel, and aluminum. International Journal of Plasticity 2012;32–33:134–54. https://doi.org/10.1016/j.ijplas.2011.11.002.
19. Preston D, Tonks D, Wallace D. Model of plastic deformation for extreme loading conditions. Journal of Applied Physics 2003;93. https://doi.org/10.1063/1.1524706.

20. Molinari A, Ravichandran G. Constitutive modeling of high-strain-rate deformation in metals based on the evolution of an effective microstructural length. Mechanics of Materials 2005;37:737–52. https://doi.org/10.1016/j.mechmat.2004.07.005.
21. Durrenberger L, Molinari A, Rusinek A. Internal variable modeling of the high strain-rate behavior of metals with applications to multiphase steels. Materials Science and Engineering: A 2008;478:297–304. https://doi.org/10.1016/j.msea.2007.06.011.
22. Durrenberger L, Molinari A. Modeling of Temperature and Strain-Rate Effects in Metals Using an Internal Variable Model. Experimental Mechanics 2009;49:247–55. https://doi.org/10.1007/s11340-008-9141-5.
23. Kocks UF, Argon AS, Ashby MF. Thermodynamics and kinetics of slip. Progress in Materials Science 1975;19:141–5.
24. Wang ZQ, Beyerlein IJ, LeSar R. Slip band formation and mobile dislocation density generation in high rate deformation of single fcc crystals. Philosophical Magazine 2008;88:1321–43. https://doi.org/10.1080/14786430802129833.
25. Gil Sevillano J, van Houtte P, Aernoudt E. Large strain work hardening and textures. Progress in Materials Science 1980;25:69–134. https://doi.org/10.1016/0079-6425(80)90001-8.
26. Nes E. Modelling of work hardening and stress saturation in FCC metals. Progress in Materials Science 1997;41:129–93. https://doi.org/10.1016/S0079-6425(97)00032-7.
27. Staker MR, Holt DL. The dislocation cell size and dislocation density in copper deformed at temperatures between 25 and 700°C. Acta Metallurgica 1972;20:569–79. https://doi.org/10.1016/0001-6160(72)90012-0.
28. Estrin Y, Kubin LP. Local strain hardening and nonuniformity of plastic deformation. Acta Metallurgica 1986;34:2455–64. https://doi.org/10.1016/0001-6160(86)90148-3.
29. Voce E. The relationship between stress and strain for homogeneous deformations 1948.
30. Hall EO. The Deformation and Ageing of Mild Steel: III Discussion of Results. Proc Phys Soc B 1951;64:747. https://doi.org/10.1088/0370-1301/64/9/303.
31. Armstrong RW. The (cleavage) strength of pre-cracked polycrystals. Engineering Fracture Mechanics 1987;28:529–38. https://doi.org/10.1016/0013-7944(87)90050-6.
32. Meyers MA, Andrade UR, Chokshi AH. The effect of grain size on the high-strain, high-strain-rate behavior of copper. Metall Mater Trans A 1995;26:2881–93. https://doi.org/10.1007/BF02669646.
33. Yan S, Yang H, Li H, Yao X. A unified model for coupling constitutive behavior and micro-defects evolution of aluminum alloys under high-strain-rate deformation. International Journal of Plasticity 2016;85:203–29. https://doi.org/10.1016/j.ijplas.2016.07.011.
34. Kocks F, Mecking H. Physics and phenomenology of strain hardening: The FCC case. Progress in Materials Science 2003;48:171–273. https://doi.org/10.1016/S0079-6425(02)00003-8.
35. Nadal M-H, Le Poac P. Continuous model for the shear modulus as a function of pressure and temperature up to the melting point: Analysis and ultrasonic validation. Journal of Applied Physics 2003;93:2472–80. https://doi.org/10.1063/1.1539913.
36. Klepaczko J, Rusinek A, Rodríguez-Martínez JA, Pęcherski R, Arias A. Modelling of thermo-viscoplastic behaviour of DH36 and Weldox 460-E structural steels at wide ranges of strain rates and temperatures, comparison of constitutive relations for impact problems. Mechanics of Materials - MECH MATER 2009;41:599–621. https://doi.org/10.1016/j.mechmat.2008.11.004.
37. Baig M, Khan AS, Choi S-H, Jeong A. Shear and multiaxial responses of oxygen free high conductivity (OFHC) copper over wide range of strain-rates and temperatures and constitutive modeling. International Journal of Plasticity 2013;40:65–80. https://doi.org/10.1016/j.ijplas.2012.07.004.
38. Mason JJ, Rosakis AJ, Ravichandran G. On the strain and strain rate dependence of the fraction of plastic work converted to heat: an experimental study using high speed infrared detectors and the Kolsky bar. Mechanics of Materials 1994;17:135–45. https://doi.org/10.1016/0167-6636(94)90054-X.
39. Voyiadjis GZ, Abed FH. Effect of dislocation density evolution on the thermomechanical response of metals with different crystal structures at low and high strain rates and temperatures. Archives of Mechanics 2005;57:299–343. https://doi.org/10.24423/aom.190.
40. Humphreys FJ, Hatherly M. Recrystallization and related annealing phenomena. 2nd ed. Amsterdam ; Boston : Elsevier; 2004.
41. Huang M, Rivera-Díaz-del-Castillo PEJ, Bouaziz O, van der Zwaag S. A constitutive model for high strain rate deformation in FCC metals based on irreversible thermodynamics. Mechanics of Materials 2009;41:982–8. https://doi.org/10.1016/j.mechmat.2009.05.007.
42. Banerjee B. Taylor impact tests: Detailed report 2005.
43. Banerjee B. An evaluation of plastic flow stress models for the simulation of high-temperature and high-strain-rate deformation of metals. 2005. https://doi.org/10.13140/RG.2.1.4289.9285.
44. Steinberg DJ, Lund CM. A constitutive model for strain rates from 10−4 to 106 s−1. Journal of Applied Physics 1989;65:1528–33. https://doi.org/10.1063/1.342968.
45. Nix WD, Gibeling JC, Hughes DA. Time-dependent deformation of metals. Metallurgical Transactions A 1985;16:2215–26. https://doi.org/10.1007/BF02670420.

 doi:10.20944/preprints202309.0828.v1